ACS APPLIED ENERGY MATERIALS

www.acsaem.org Article

Ultrastable Porous Organic Polymers Containing Thianthrene and Pyrene Units as Organic Electrode Materials for Supercapacitors

Mohamed Gamal Mohamed,*,¶ Swetha V. Chaganti,¶ Meng-Syuan Li, Maha Mohamed Samy, Santosh U. Sharma, Jyh-Tsung Lee, Mohamed Hammad Elsayed, Ho-Hsiu Chou, and Shiao-Wei Kuo*

Cite This: *ACS Appl. Energy Mater.* 2022, 5, 6442−6452 Read Online

ACCESS | Metrics & More | Article Recommendations | Supporting Information

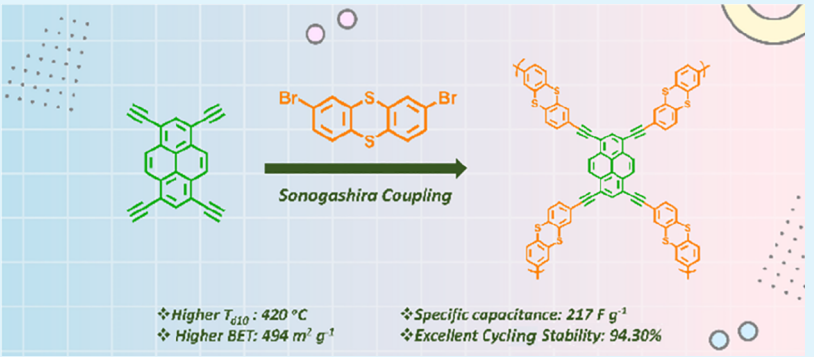

ABSTRACT: In this study, we successfully synthesized, designed, and constructed three porous organic polymers (POPs) without or with acetylene as the bridge—Bz-Th, TPA-Th, and P-Th-POPs—through a robust and efficient coupling reaction of 2,8-dibromothianthrene (Th-Br_2) as a building unit with 1,3,5-tris(4,4,5,5-tetramethyl-1,3,2-dioxaborolan-2-yl)benzene (Bz-3BO), tris(4-(4,4,5,5-tetramethyl-1,3,2-dioxaborolan-2-yl)phenyl)amine (TPA-3BO), and 1,3,6,8-tetraethynylpyrene (P-T). Our POP materials displayed exceptional heat stability (char yields of more than 70% for each POP) and superior Brunauer−Emmett−Teller surface areas. According to electrochemical testing, a P-Th-POP-containing acetylene group as a bridge has a specific capacitance of 217 F g^{-1} at 0.5 A g^{-1} and an excellent cycling stability of over 5000 times at 10 A g^{-1}. Compared to other porous materials, P-Th-CMP exhibits the highest specific capacitance, which may be attributed to its enormous surface area and extended conjugation system.

KEYWORDS: *thianthrene, porous organic polymers, Suzuki coupling, Sonogashira coupling, thermal stability, electrochemical performance*

INTRODUCTION

Energy is an essential requirement for the human civilization's survival and progress. The demand for conventional fossil fuels is growing in tandem with the fast expansion of the economy and society and the increase in significant environmental pollution.[1−4] As an energy carrier, electric energy may be created from clean and renewable resources such as solar, tidal, or wind energy and shows much promise in satisfying our needs for long-term energy. However, dependency on these renewable resources is not a good idea as they provide energy as per the availability of the raw materials, which are depleting. Besides this, the increase in global warming is evidence that fossil fuels also affect the environment through consistent carbon dioxide (CO_2) emissions.[5,6] As a result, it is vital to design some effective technologies to stockpile energy and address the current issues. Supercapacitors are often used for their effectiveness in energy storage, high power density, cycling stability, higher energy density, a longer cycling life, and a faster charge/discharge rate than that of ordinary dielectric capacitors[7,8] and hence are ideal choices for electronic and electrical appliances.[9−11] The supercapacitor has a larger power output than a secondary battery (0.5−10 kW kg^{-1}) but a lower power output than a capacitor. Nonetheless, the supercapacitor has the highest specific energy. Supercapacitors get the luxury of gaining an excellent power value even at 40 °C, which batteries lack.[12] Another advantage of supercapacitors is their ability to supply tremendous power safely (during the charging−discharging process).[13] The primary advantage of supercapacitors is their high stability, which is due to their charge holding process; because it is reversible, the charging−discharging action does not lead to a

Received: March 28, 2022
Accepted: April 21, 2022
Published: May 3, 2022

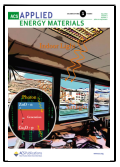

https://doi.org/10.1021/acsaem.2c00942
ACS Appl. Energy Mater. 2022, 5, 6442−6452

difference in the electrode volume.[11] In opposition to the cloud to store a battery charge, most of the material undergoes an irrevocable redox reaction. The main drawback of supercapacitors is their small working potential window.[14] When the applied voltage is too high, the electrolyte decomposes.[12] Although supercapacitors have disadvantages, advances in polymer research have overcome these constraints.[5] Supercapacitors are classified into three types, based on the charge storage mechanism: electric double-layer capacitors (EDLCs), electrochemical pseudocapacitors, and hybrid supercapacitors.[8,12,15−17]

Covalent organic polymers (COPs) are attractive porous materials for a wide range of applications, including pollutant removal, sensors, CO_2 capture, storage, separation, drug administrations, catalysis, SO_2 adsorption, genetic manipulation, Li−S batteries, energy conversion, and light harvesting. When contrasted to metal−organic frameworks, they have several notable properties, such as large temperature durability, high Brunauer−Emmett−Teller (BET) surface areas, approachable permeability, large pore diameters, chemical inertness, nontoxicity, and improved electrical conductivity.[18−42] Covalent organic frameworks,[41,42] porous imine-linked networks, benzimidazole-linked polymers, covalent triazine frameworks,[40] porous aromatic frameworks, carbazole-based microporous polymers, and hyper-cross-linked porous polymers,[43,44] conjugated microporous polymers (CMPs),[45−51] metal−organic frameworks,[30,48,49] and ferrocene-based CMPs[52] are examples of COP materials.[39] CMPs are a form of porous organic polymers (POPs) with a microporous structure that includes π-conjugation.[53−64] Because of the broad spectrum of essential components and reactions available, CMP materials could have a variety of structures and properties. CMPs, for example, have been produced utilizing both conventional coupling processes (such as Sonogashira−Hagihara, Suzuki−Miyaura, and Yamamoto coupling) and oxidative polymerization.[23−25]

CMPs have a variety of desirable properties, including simplicity of preparation, high surface area, permeability, intense sensitivity to visible light, remarkable thermal resilience, and superior optoelectronic capabilities.[65] Consequently, CMPs might be useful in separation processes, solar fuel production, electricity storage, metal ion sensing, gas adsorption, photocatalytic H_2 production, and photoredox catalysis.[26−34,39] Furthermore, adding heteroatoms (N, P, S, etc.) enhances electron density, improves the exposed area, and boosts the ion diffusion rate, and hence, the supercapacitor performance may be significantly improved.[17,35−38] More physically customizable porous materials with an enormous surface area, a high heteroatom concentration, and pseudocapacitive features must be created to increase the capacitance attributes of supercapacitors.[8] By understanding the specific requirements, three thianthrene-based POPs were prepared using the Suzuki and Sonogashira coupling reaction, namely, Bz-Th-POP, TPA-Th-POP, and P-Th-POP. The effect of heteroatoms (N and S) on extended conjugation and porosity have been studied. This research opens gates for us to use a thianthrene (Th) moiety as an electrode in supercapacitors.

EXPERIMENTAL SECTION

Materials. Thianthrene (Th), acetic acid, bromine solution (Br_2), sodium hydrogen carbonate ($NaHCO_3$), tribromobenzene (Bz-Br_3), potassium acetate (KOAc), *N*-bromosuccinimide (NBS), triphenylamine (TPA), pyrene, nitrobenzene, triphenylphosphine (PPh_3), $Pd(PPh_3)_4$, copper(I) iodide (CuI), $Pd(dppf)Cl_2$, and magnesium sulfate anhydrous ($MgSO_4$) were purchased from Sigma-Aldrich. Potassium carbonate (K_2CO_3, 99.99%) was ordered from Alfa Aesar. Dichloromethane (DCM), methanol (MeOH), 1,4-dioxane, hexane, ethyl acetate (EA), triethylamine (Et_3N), toluene, and acetone were purchased from Acros. Bis(pinacolato)dibron (B_2pin_2) was bought from J. T. Baker. P-T was synthesized using procedures reported previously [Figures S1−S3].

Synthesis of Th-Br_2. In a 100 mL round-bottom flask, thianthrene (2.16 g, 10 mmol), acetic acid (40 mL), and a solution of bromine (4 mL) were added slowly. The mixture was heated up to 80 °C for 16 h. After the reaction, deionized (DI) water (20 mL) was added to afford a white solid. Then, the mixture was rinsed with $NaHCO_3$ (5%) and recrystallized with methanol and DCM to obtain Th-Br_2 (1.90 g, 88%, Scheme S1). Fourier transform infrared (FTIR) (Figure S4): 3066 cm^{-1}. ^1H NMR (Figure S5): 7.71, 7.62, 7.31 ppm. ^{13}C NMR (Figure S6): 138−122.44 ppm.

Synthesis of 1,3,5-Tris(4,4,5,5-tetramethyl-1,3,2-dioxaborolan-2-yl)benzene (Bz-3BO). In a 100 mL round-bottom flask, 50 mL of 1,4-dioxane, Bz-Br_3 (0.50 g, 1.59 mmol), bis(pinacolato)dibron (1.33 g, 5.24 mmol), $Pd(dppf)Cl_2$ (0.06 g, 0.079 mmol), and KOAc (0.99 g, 10.09 mmol) were added. After that, the mixture was heated for 48 h at 80 °C. After the completion of the reaction, the mixture was extracted with EA. The obtained residue was purified using column chromatography to afford Bz-3BO as a white solid (0.42 g, 84%, Scheme S2). FTIR (Figure S7): 2983, 1599, 1319 (B−O), 1139, 964, 892 cm^{-1}. ^1H NMR (Figure S8): 8.36 (s, 3H), 1.34 (s, 36H) ppm. ^{13}C NMR (Figure S9): 145, 84.29, 25.17 ppm.

Synthesis of Tris(4-bromophenyl)amine (TPA-Br_3). NBS (2.00 g, 11.50 mmol) and TPA (0.92 g, 3.79 mmol) were dissolved in dimethylformamide (DMF) (40 mL), and the mixture was stirred for 24 h. After removing DMF, the mixture was extracted with CH_2Cl_2 and DI water. $MgSO_4$ was then added into the mixture to dry the organic layer and removed using the filter. The residue was rinsed with MeOH several times to acquire TPA-Br_3 (0.94 g, 90%, Scheme S3). FTIR (Figure S10): 3078, 1618 (C=C) cm^{-1}. ^1H NMR (Figure S11): 7.35 (s, 3H), 6.93 ppm. ^{13}C NMR (Figure S12): 146.66, 133.09, 126.10, 116.44 ppm.

Synthesis of Tris(4-(4,4,5,5-tetramethyl-1,3,2-dioxaborolan-2-yl)phenyl)amine (TPA-3BO). In round-bottom flask, KOAc (70 mmol), 60 mL of 1,4-dioxane, TPA-Br_3 (4 mmol), B_2pin_2 (15 mmol), and $Pd(dppf)Cl_2$ (0.68 mmol) were added. The solution was heated for 48 h at 85 °C. After the completion of the reaction, the mixture was extracted with DCM and DI water. $MgSO_4$ was then added into the mixture to dry the organic layer and removed using the filter. The resulting residue was purified using hexane/EA (2/1) as an eluent to obtain a creamy yellow solid (0.81 g, 42%, Scheme S4). FTIR (Figure S13): 2981, 1585.33, 1359.37 (B−O), 1308.90, 1141.70 cm^{-1}. ^1H NMR (Figure S14): 7.67, 7.06, 1.36 (s, 36H) ppm. ^{13}C NMR (Figure S15): 150.7, 136.55, 123.71, 123.33, 83.74, 22.86 ppm.

Synthesis of Bz-Th-POP. Th-Br_2 (0.184 g, 0.49 mmol), Bz-3BO (0.15 g, 0.33 mmol), K_2CO_3 (0.364 g, 2.63 mmol), $Pd(PPh_3)_4$ (0.02 g, 0.013 mmol), DMF (8 mL), and DI water (2 mL) were placed in a flame-dried Schlenk tube. The mixture was subjected to three freeze/pump/thaw cycles and heated to 90 °C for 3 days. The solid was filtered and rinsed with various organic solvents to remove the residual reagents. The solid was then dried at 60 °C overnight to acquire Bz-Th-CMP as a light gray powder (0.14 g, Scheme S5).

Synthesis of TPA-Th-POP. In a flame-dried Schlenk tube, Th-Br_2 (0.18 g, 0.48 mmol), TPA-3BO (0.20 g, 0.32 mmol), K_2CO_3 (0.36 g, 2.56 mmol), $Pd(PPh_3)_4$ (0.07 g, 0.057 mmol), DMF (8 mL), and DI water (2 mL) were added. The solid was then dried at 60 °C overnight to give TPA-Th-CMP as a dark gray powder (0.08 g, Scheme S6).

Synthesis of P-Th-POP. P-Th-POP was prepared using a method similar to the Bz-Th-POP method: In a flame-dried Schlenk tube, P-T (0.15 g, 0.5 mmol), Th-Br_2 (0.37 g, 0.99 mmol), CuI (0.001 g, 0.05 mmol), PPh_3 (0.013 g, 0.05 mmol), $Pd(PPh_3)_4$ (0.06 g, 0.05 mmol), DMF (5 mL), and Et_3N (5 mL) were added. The solid was then dried

https://doi.org/10.1021/acsaem.2c00942
ACS Appl. Energy Mater. 2022, 5, 6442−6452

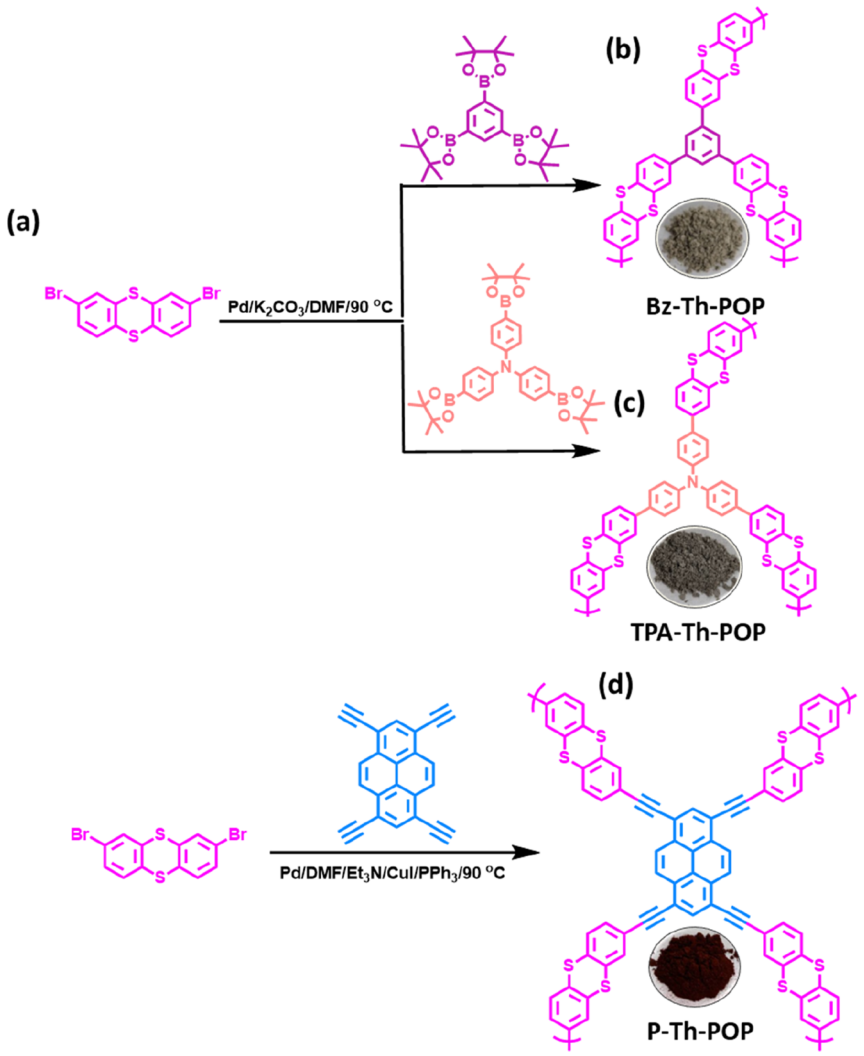

Figure 1. Synthesis of Bz-Th (b), TPA-Th (c), and P-Th-POPs (d) from Th-Br_2 (a).

at 60 °C overnight to afford P-Th-CMP as a dark red powder (0.29 g, Scheme S7).

RESULTS AND DISCUSSION

Synthesis and Characterization of Th-POPs. Th-POPs materials were synthesized in this work through two different coupling reactions, as shown in Figure 1. First, Bz-Th-POP and TPA-Th-POP were prepared using the Suzuki coupling reaction of Th-Br_2 [Figure 1a] with Bz-3BO and TPA-3BO in the presence of Pd and K_2CO_3 [Figure 1b,c]. Second, P-Th-POP was prepared through a Sonogashira coupling reaction of Th-Br_2 with P-T in the mixture of a DMF/Et_3N solution and Pd as a catalyst [Figure 1d].

Figure 2a exhibits the FTIR spectra of Th-POPs at room temperature, which depict the absorption signals of all Th-POPs in the region of 1450−1590 and 3030 cm^{-1} for the C=C aromatic groups and the C−H aromatic groups, respectively. The disappearance of the absorption band of the C−Br group and B−O bonds following the reaction is attributable to the effective development of cross-linked networks. Moreover, the band related to the terminal alkynyl group in P-Th-POP appeared at 2196 cm^{-1}. We observed that the absorption band near 3411 cm^{-1} in both Bz and P-Th-POP samples was ascribed to water adsorbed by these two porous materials.

Solid-state ^{13}C nuclear magnetic resonance (NMR) spectroscopy was also performed to obtain the Th-POP structures. Figure 2b shows that all Th-POP materials showed carbon signals in the range 139.65−114.81 ppm attributed to the phenyl groups. The alkyne groups belong to the resonance peak near 80.26 ppm in the P-T-POP spectrum. In this experiment, the carbon, nitrogen, hydrogen, and sulfur contents of Bz-Th, TPA-Th, and P-Th-POPs are determined using elemental analyses and sorted in Table S1. The high sulfur contents in all Th-POP samples indicated the successful fusion of the Th moiety in the POPs frameworks. In conclusion, the NMR, FTIR spectroscopy, and elemental analysis powerfully confirmed the successful preparation of Th-POPs. Thermogravimetric analysis (TGA) studies were used to determine the thermal stabilities of Th-POPs in a nitrogen environment at 20 °C min^{-1}. Figure 2c demonstrates that the declining thermal curves imply weight reduction. TGA measurements indicate that T_{d5}, T_{d10}, and char yield values for Bz-Th-POP are 308 °C, 500 °C, and 71%, respectively, and 498 °C, 577 °C, and 81% for TPA-Th-POP, respectively, whereas the values are 345 °C, 420 °C, and 70% for P-Th-POP, respectively. Our porous materials have been shown to have good thermal stability. Table 1 summarizes the T_{d5}, T_{d10}, and char yield values for Th-POP materials. All Bz-Th-POP

https://doi.org/10.1021/acsaem.2c00942
ACS Appl. Energy Mater. 2022, 5, 6442−6452

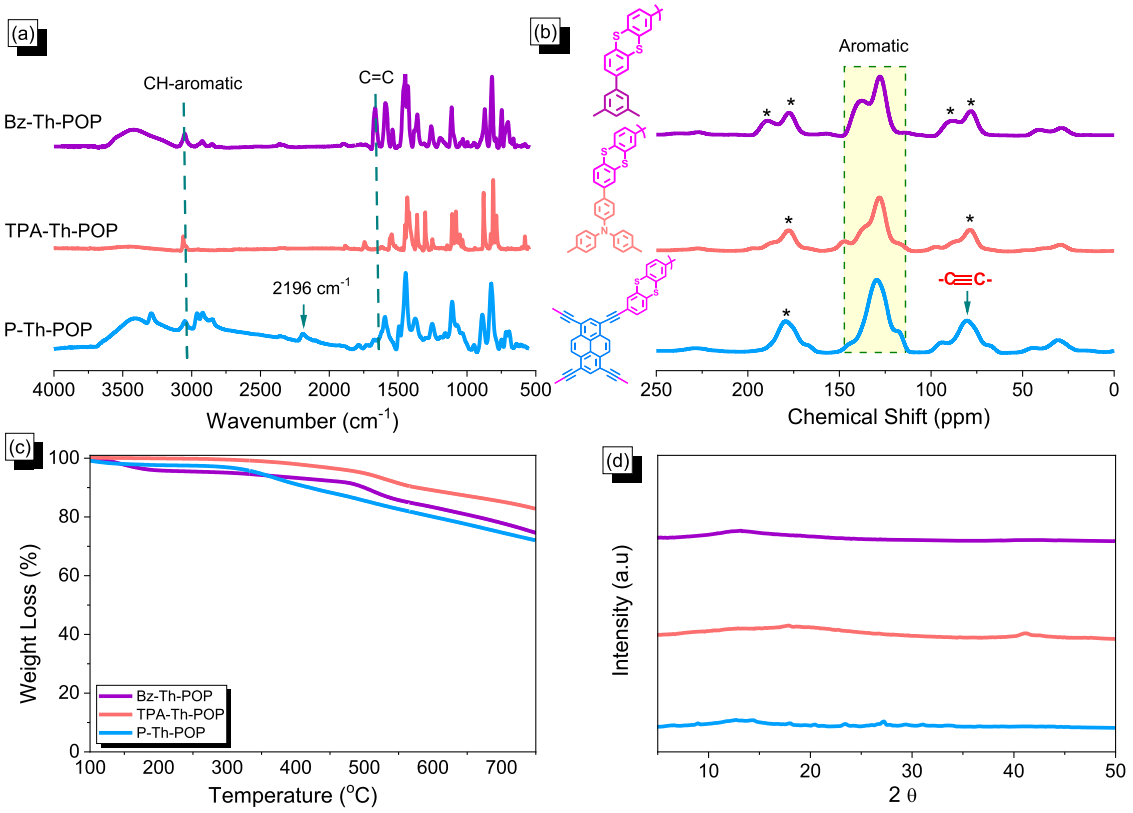

Figure 2. FTIR spectra (a), ^{13}C NMR spectra (b), TGA curves (c), and XRD patterns (d) of Bz-Th, TPA-Th, and P-Th-POPs.

Table 1. Summarized TGA, BET, and Capacitance Data of B-Th, TPA-Th and P-Th-POPs

sample	T_{d5} (°C)	T_{d10} (°C)	char yield (wt %)	surface area (m^2/g)	pore volume (cm^3/g)	pore size (nm)	capacity at 0.5 A g^{-1} (F g^{-1})
Bz-Th-POP	308	500	71	112	0.41	1.80	87
TPA-Th-POP	498	577	81	73	0.24	2.05	107
P-Th-POP	345	420	70	494	0.61	1.40	217

and TPA-Th-POP materials showed an amorphous character, and the P-Th-POP sample had semicrystalline properties, as revealed in the X-ray diffraction (XRD) profile (Figure 2d).

Nitrogen adsorption/desorption measurements at 77 K corroborated the porosity features of the three as-prepared CMPs (Figure 3a and Table 1). Before the analyses, the Th-POP samples were degassed under vacuum at 150 °C for 12 h. According to the IUPAC classification, these data indicate that Bz-Th-POP and TPA-Th-POP had type III adsorption isotherms. In contrast, P-Th-POP had type I with type IV adsorption isotherms. Furthermore, the BET profile of P-Th-POP shows that the N_2 uptake capacity was enhanced at low- and high-pressure areas, indicating the presence of micro- and mesopores in the P-Th-POP frameworks. The specific surface area of P-Th-CMP (494 m^2 g^{-1}) was among the highest of the as-prepared POPs (112 m^2 g^{-1} for Bz-Th-POP and 73 m^2 g^{-1} for TPA-Th-POP). The pore size distributions of Bz-Th-CMP, TPA-Th-CMP, and P-Th-CMP were estimated using the nonlocal density functional theory, yielding micropore and mesopore diameters of 1.80, 2.05, and 1.40 nm, respectively (Figure 3b and Table 1). The total pore volume for Bz-Th-CMP was 0.41, 0.24 cm^3 g^{-1} for TPA-Th-POP, and 0.61 cm^3 g^{-1} for P-Th-CMP.

The morphology, ordering, and porosity characteristics of Bz-Th-POP, TPA-Th-POP, and P-Th-CMP were observed using scanning electron microscopy (SEM) and high-resolution transmission electron microscopy (HR-TEM), as shown in Figure 4, respectively. According to SEM measurements (Figure 4a–c), Bz-Th-CMP generated irregular nanospheres and rods, TPA-Th-POP created primarily clusters of aggregated nanospheres, and P-Th-POP formed urchin-like spheres with hairy surfaces. The HR-TEM images, as shown in Figure 4d–f, also imply no long-range ordering and porous character of the as-prepared POPs.

Supercapacitor Performance of Th-POP Materials. The electrochemical performance of all Th-POPs was assessed using cyclic voltammetry (CV) and galvanostatic charge/discharge (GCD) profiles in an aqueous solution of 1.0 M KOH with a three-electrode system composed of glassy carbon, platinum, and Hg/HgO as the working, counter, and reference electrodes, respectively. Figure 5a–c shows the CV curves of Bz-Th, TPA-Th, and P-Th-POPs, respectively, within a potential range of −1.0–0.0 V (vs Hg/HgO) for a broad range of scan rates from 5 to 200 mV s^{-1}. It is pretty evident that the typical rectangle-like humped shape has been obtained for all the Th-POPs, which remained consistent with scan sweeping, proving that the as-obtained POPs are stable with respect to the current sweep and portray capacitance from EDLCs.[45,66] The better coherence of P-Th-POP's CV curves over various scan rates can be explained by its high specific surface area and electron-rich phenyl groups. The abundance of the heteroatoms and unique morphologies structures in the

https://doi.org/10.1021/acsaem.2c00942
ACS Appl. Energy Mater. 2022, 5, 6442–6452

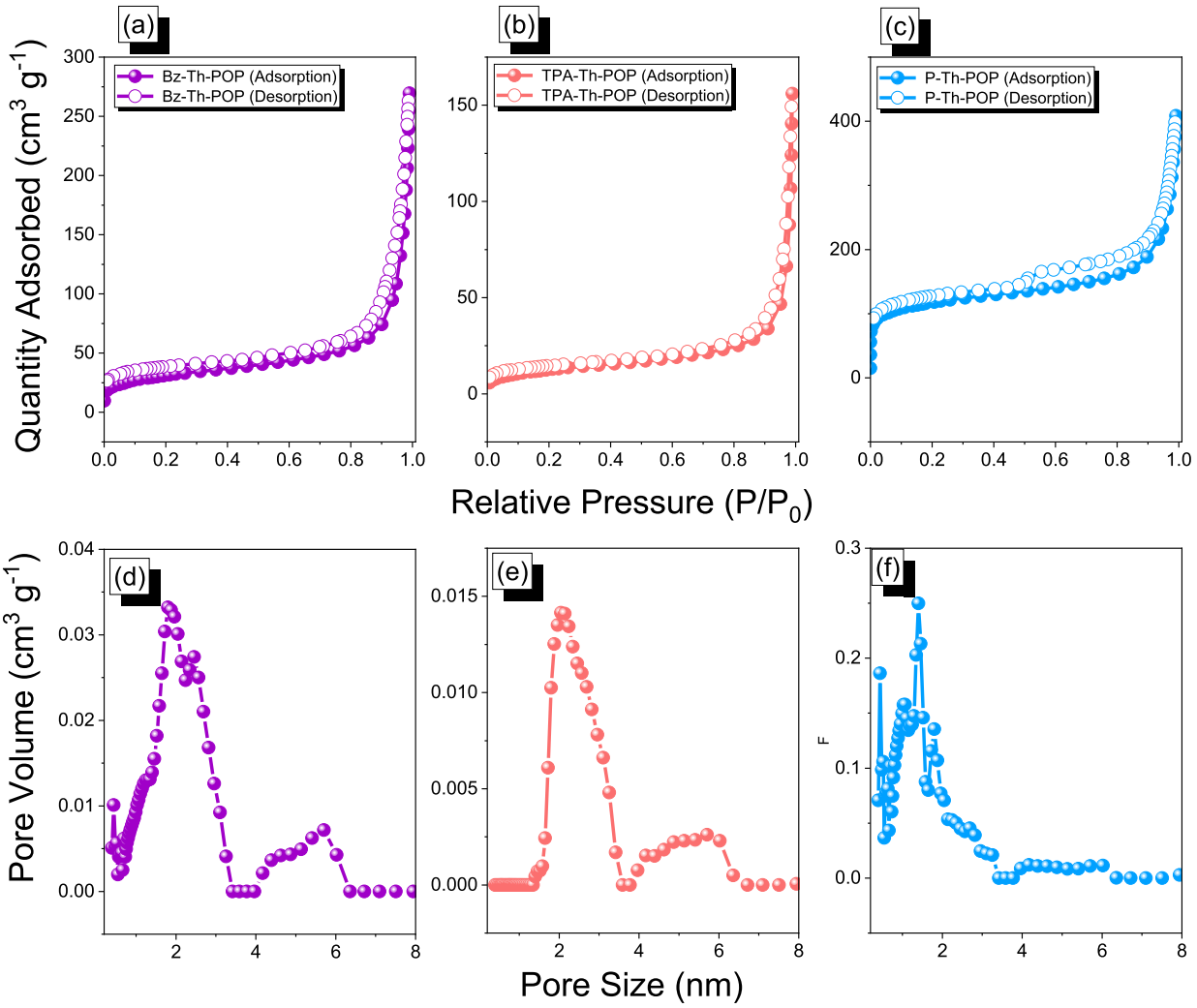

Figure 3. N_2 sorption and pore size distribution profiles of Bz-Th (a,d), TPA-Th (b,e), and P-Th-POPs (c,f), were recorded at 77 K.

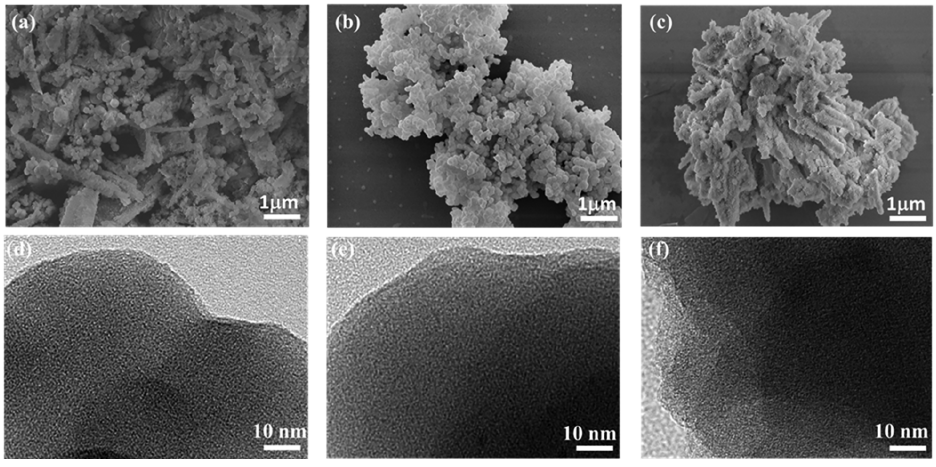

Figure 4. SEM and TEM images of Bz-Th (a,d), TPA-Th (b,e), and P-Th-POPs (c,f).

POPs can be thanked for the pseudocapacitance because they enabled efficient electron transferring by forming better contact with the electrolyte.[8,13] The CV curves reveal the strong rate capability and simple kinetics of these POPs. Furthermore, these compounds' charge/discharge profiles and capacitance were checked at current densities ranging from 0.5 to 20 A g^{-1} (Figure 5d–f). The GCD curve for all the compounds shows a bent triangular shape, which indicates pseudocapacitive and EDLC characteristics. Heteroatoms can reason a bent shape in the molecules.[3,7] When we compare the charging and discharging times, the discharge time is higher than the charging time for all the POPs, indicating improved capacitance.[3,7] Among the three POPs, P-Th-POPs displayed a

https://doi.org/10.1021/acsaem.2c00942
ACS Appl. Energy Mater. 2022, 5, 6442−6452

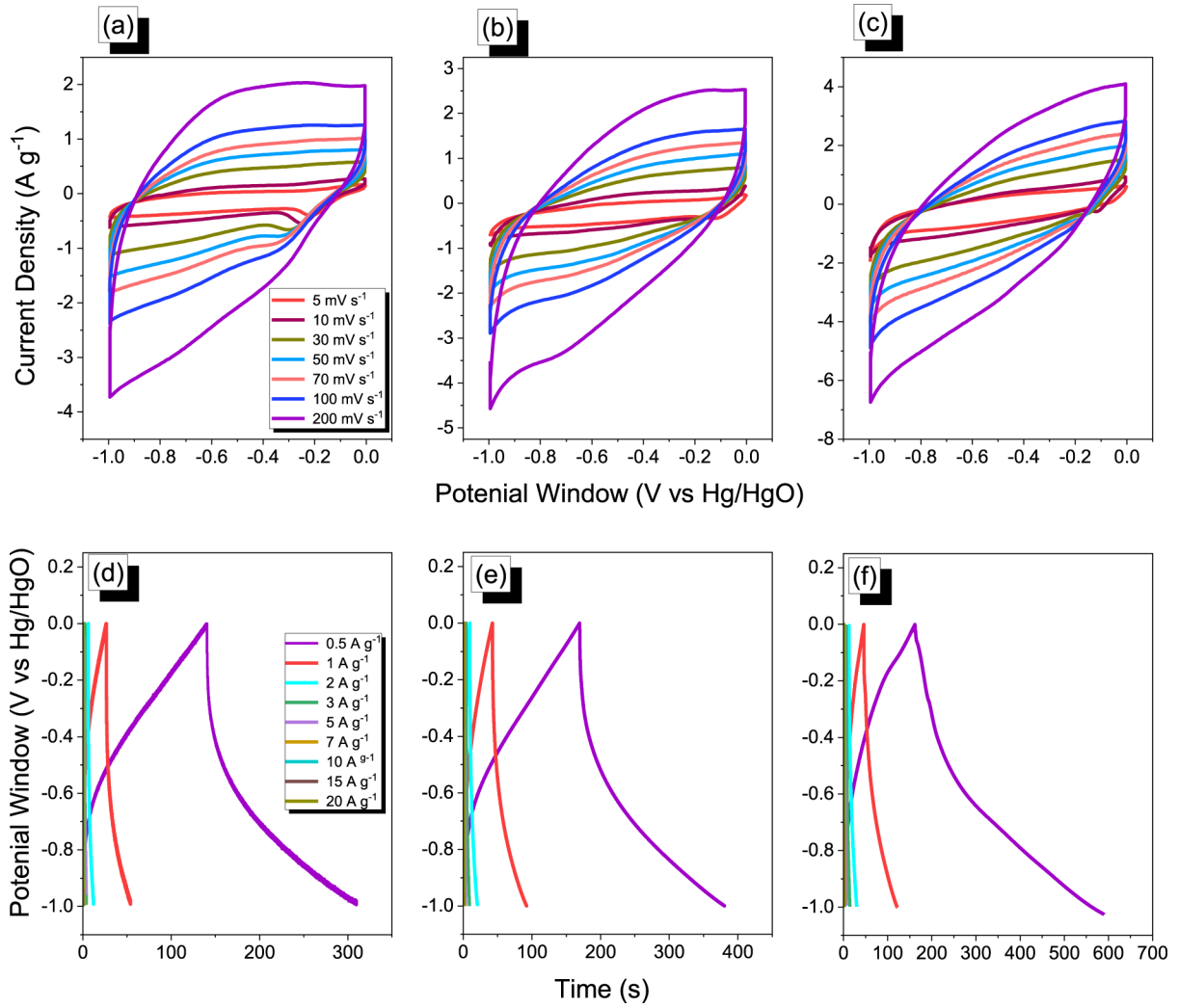

Figure 5. CV and GCD profiles of Bz-Th (a,d), TPA-Th (b,e), and P-Th-POPs (c,f).

longer discharge time, indirectly related to the higher capacitance (Figure 5f).

The specific capacitance was measured and is displayed in Figure 6a. At the current density of 0.5 A g^{-1}, the capacitance values of Bz-Th, TPA-Th, and P-Th-POPs were 87, 107, and 217 F g^{-1}, respectively. Thus, the capacitance of P-Th-POP was 3-fold that of the other two POPs, and the difference remained consistent till a higher current density of 20 A g^{-1}, where the capacitance values of Bz-Th-POP, TPA-Th-POP, and P-Th-POP were 0.5, 5, and 8.3 F g^{-1} respectively. The superior performance of P-Th-POP can be explained based on its structure. The benzene rings in the pyrene molecule form $\pi-\pi$-stacking, enabling it to form a good structure for electrochemical activity and conductivity due to electron distribution and enhancing its porosity for the mitigation of the electrolyte. The increase in the capacitance of TPA-Th-POP in comparison to that of Bz-Th-POP can be attributed to the presence of an additional heteroatom (N) in the core, allowing electrolytes to reach the electrode surface more quickly. The curiosity about the stability of the POPs was aroused, and the cycling stability was examined for 5000 cycles at a current density of 10 A g^{-1}(Figure 6b). The capacity retention of the POPs is in the decreasing order of P-Th-POP, TPA-Th-POP, and Bz-Th-POP, with the retention values of 99.46, 97.67, and 94.19%, respectively. These results reveal that these compounds are stable for long cycles, even at a high current density. Furthermore, the P-Th-POP material displayed a higher energy density value (29.94 W h kg^{-1}) than the other two materials—TPA-Th-POP (14.89 W h kg^{-1}) and Bz-Th-POP (12.31 W h kg^{-1}) (Figure 6c). Figure 6d shows that P-Th-POP has excellent electrochemical performance and high specific capacitance compared to other POP precursors. Further, electrochemical impedance spectroscopy was employed to study the electric resistance offered from different electrodes through the ion diffusion mechanism. Figure 7a represents the different Nyquist plots with the equivalent fitted circuits (Figure 7b and Table 2) to compare the different properties such as series and charge transfer from the electrodes. In the fitted circuit, R_s, R_{ct}, CPE−EDL, CPE-P, and Z_w represent the equivalent series resistance, charge transfer resistance, constant phase elements representing EDLC behavior and pseudocapacitive behavior, and Warburg element, respectively. As per Table 2, the initial series resistance known as Ohmic resistance values of all of the electrodes are 2, 5, and 1 Ω for Bz-Th-POP, TPA-Th-POP, and P-Th-POP, respectively. In addition to this, the charge transfer values for Bz-Th-POP, TPA-Th-POP, and P-Th-POP electrodes were 28, 18.2, and 9 Ω, respectively. Thus, among all of these electrodes, the P-Th-POP delivers the smallest

https://doi.org/10.1021/acsaem.2c00942
ACS Appl. Energy Mater. 2022, 5, 6442−6452

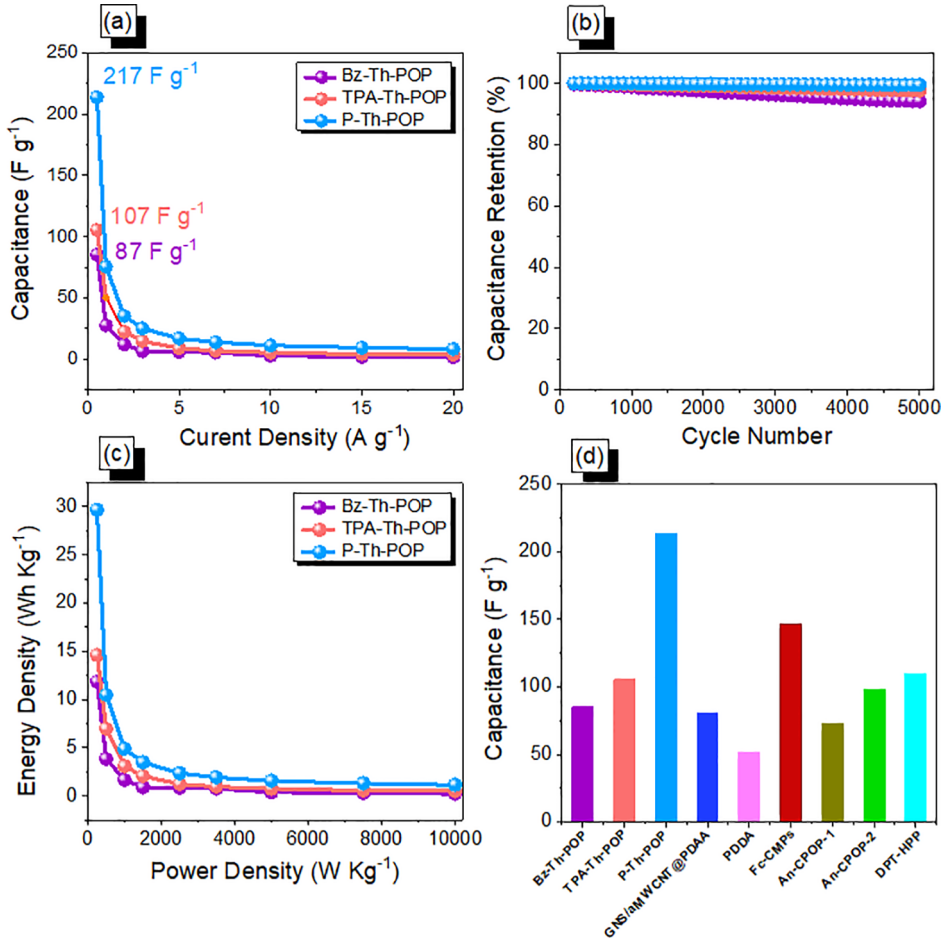

Figure 6. Specific capacitance (a), durability (b), and Ragone (c) profiles of Bz-Th TPA-Th, and P-Th-POPs. (d) Comparison of electrochemical performances of three Th-POP samples with others reported materials.

Ohmic and charge transfer resistances and thus is the superior conductive material compared to others.

Apart from this, Figure 7c represents the Bode plot of the frequency-dependent magnitude. The figures reveal slant lines with a negative slope at low frequency and small resistances at high frequency, demonstrating excellent capacitive characteristics of the electrode materials. On the other hand, Figure 7d shows different electrodes' frequency-dependent phase angle plots. From this figure, the knee frequencies were evaluated at a phase angle of −45°, where the capacitive and resistive behaviors of electrodes are equal. The knee frequencies for Bz-Th-POP, TPA-Th-POP, and P-Th-POP were 89.21, 117.07, and 311.87 Hz, respectively. The knee frequency is directly proportional to the rate performance. It has been reported that a higher knee frequency is often associated with a better rate performance. Thus, P-Th-POP delivered an outstanding performance as an electrode for energy storage materials compared to Bz-Th-POP and TPA-Th-POP. Further, above the knee frequency, the supercapacitor becomes more resistive, where the diffusion of electrolyte ions starts within the porous network structure.[67−70]

Furthermore, we have evaluated the electrochemical performance of an asymmetric supercapacitor device of Th-POP samples using a CR2032 coin cell. The electrochemical performances were carried out in the potential range of −1.0−0 V. The CV profiles were recorded at different scan rates between 5 and 200 mV s^{-1}, as shown in Figure S16a−c for P-Th-POP, TPA-Th-POP, and Bz-Th-POP, respectively. The curves of all of the electrodes were nearly rectangular with humps in the lower potential range, which is a typical behavior of supercapacitors attributed to the pseudocapacitive and double-layer capacitive natures. Upon increasing the scan rates, the integrity of electrodes was relatively stable, demonstrating the increase in the current density, which exhibits a better rate of capability and stability of electrode materials. In addition, the GCD curves for the P-Th-POP, TPA-Th-POP, and Bz-Th-POP electrodes are shown in Figure S16d−f, respectively, at current densities between 0.5 and 20 A g^{-1}. The curves represent the almost triangular nature with the presence of a bent curve arising from the heteroatoms in the structure, suggesting the combined effect of pseudocapacitance and electric double-layer capacitance. The specific capacitance was calculated from the GCD curves at a current density of 0.5 A g^{-1}. The values for specific capacitance were 116.5, 21.5, and 30.9 F g^{-1} for P-Th-POP, TPA-Th-POP, and Bz-Th-POP electrodes, respectively. Thus, it can be observed that the P-Th-POP electrode exhibited superior capacitance compared to TPA-Th-POP and Bz-Th-POP. This superior performance of the P-Th-POP material can be attributed to the highest surface area of P-Th-POP, which eases the mobility of ions and thus increases the rate capability and stability of electrodes. Figure S17 shows the glowing light-emitting diode (LED) photograph with the P-Th-POP asymmetric coin supercapacitor.

https://doi.org/10.1021/acsaem.2c00942
ACS Appl. Energy Mater. 2022, 5, 6442−6452

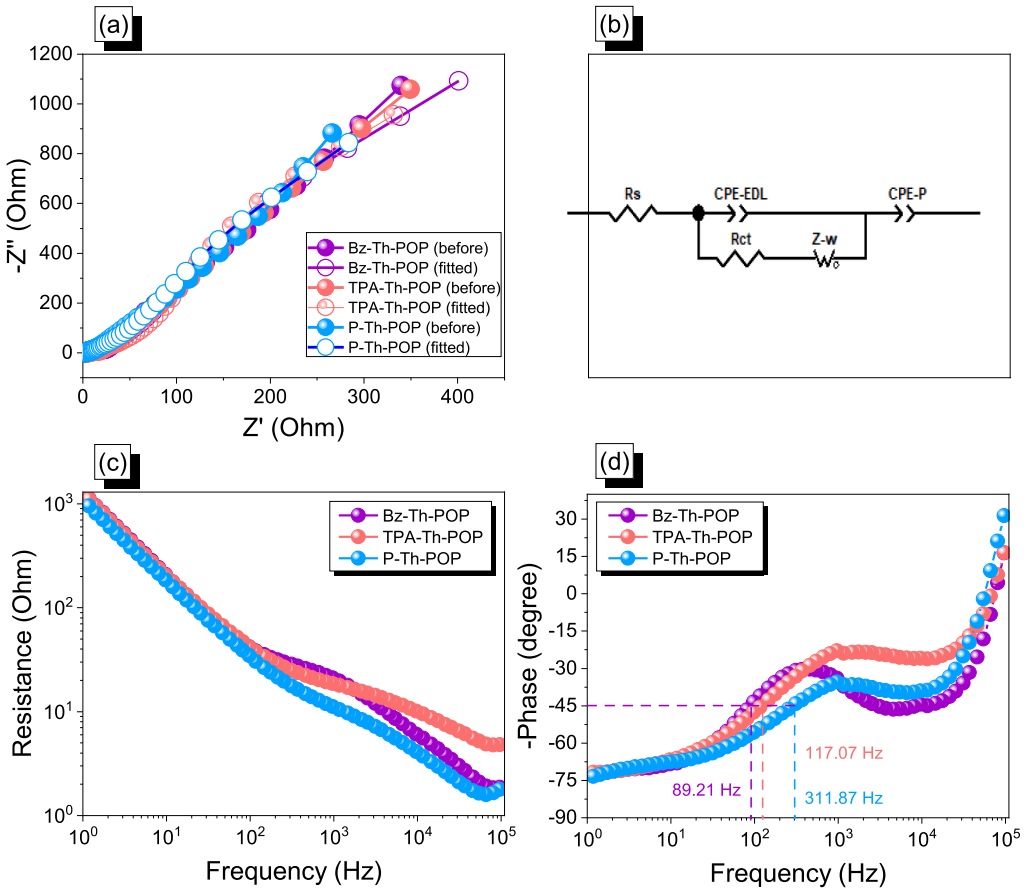

Figure 7. (a) Nyquist plots, (b) equivalent fitted circuit, (c) Bode plots of the frequency-dependent magnitude, and (d) Bode plots of the frequency-dependent phase angle of Bz-Th-POP, TPA-Th-POP, and P-Th-POP.

Table 2. Values for the Equivalent Fitted Circuit of Nyquist Plots

sample	R_s (Ω)	R_{ct} (Ω)	CPE-EDL (S s^n)	CPE-P (S s^n)
Bz-Th-CMP	2	28	8.01×10^{-5}	0.00078
TPA-Th-CMP	5	18.2	8.01×10^{-5}	0.00083
P-Th-CMP	1	9	12.01×10^{-5}	0.00081

CONCLUSIONS

The successful synthesis of thianthrene-based POPs has been obtained via simple coupling reactions. The as-prepared POPs were characterized by heteroatoms and the extended π-conjugation (in the case of P-Th-POP). Their influence on the performance as an electrode material for supercapacitors has been explored. The prepared POPs portrayed high thermal stability, porosity, and specific surface areas. The electrochemical properties were investigated, and it revealed typical ELDC and pseudocapacitance behaviors, high capacitance, and a high cycling stability of up to 2000 cycles. Among the three POPs, P-Th-POP displayed a high capacitance of 217 F g^{-1} at 0.5 A g^{-1} with a 99.46% capacity retention after 5000 cycles. The excellent performance compared to that of the other two POPs can be attributed to the synergism between heteroatoms and the extended π-conjugation, which results in electrostatic coupling, charge delocalization, and better wettability. These results promote the exploration of thianthrene-type molecules for application in supercapacitors.

ASSOCIATED CONTENT

Supporting Information

The Supporting Information is available free of charge at https://pubs.acs.org/doi/10.1021/acsaem.2c00942.

Details about characterization methods and electrochemical analysis; elemental analyses of Bz-Th-CMP, TPA-Th-CMP, and P-Th-CMP; synthetic routes for the preparation of Th-Br_2; synthetic routes for the preparation of Bz-3BO; synthetic routes for the preparation of TPA-Br_3; synthetic routes for the preparation of TPA-3BO; synthetic routes for the preparation of Bz-Th-POP; synthetic routes for the preparation of TPA-Th-POP; synthetic routes for the preparation of P-Th-POP; FTIR profile of P-T; ^{1}H NMR spectrum of P-T in $CDCl_3$; ^{13}C NMR spectrum of P-T in $CDCl_3$; FTIR profile of Th-Br_2; ^{1}H NMR spectrum of Th-Br_2 in $CDCl_3$; ^{13}C NMR spectrum of Th-Br_2 in $CDCl_3$; FTIR profile of Bz-3BO; ^{1}H NMR spectrum of Bz-3BO in $CDCl_3$; ^{13}C NMR spectrum of Bz-3BO in $CDCl_3$; FTIR profile of TPA-Br_3; ^{1}H NMR spectrum of TPA-Br_3 in $CDCl_3$; ^{13}C NMR spectrum of TPA-Br_3 in $CDCl_3$; FTIR profile of TPA-3BO; ^{1}H NMR spectrum of TPA-3BO in $CDCl_3$; ^{13}C NMR spectrum of TPA-3BO in $CDCl_3$; electrochemical performance of an asymmetric supercapacitor device of Th-POPs and CV and GCD profiles of P-Th, TPA-Th, and Bz-Th-POPs; and the glowing LED photograph with a P-Th-POP asymmetric coin supercapacitor (PDF)

https://doi.org/10.1021/acsaem.2c00942
ACS Appl. Energy Mater. 2022, 5, 6442−6452

AUTHOR INFORMATION

Corresponding Authors

Mohamed Gamal Mohamed − *Department of Materials and Optoelectronic Science, Center for Functional Polymers and Supramolecular Materials, National Sun Yat-Sen University, Kaohsiung 804, Taiwan; Department of Chemistry, Faculty of Science, Assiut University, Assiut 71516, Egypt;* orcid.org/0000-0003-0301-8372; Email: mgamal.eldin12@yahoo.com

Shiao-Wei Kuo − *Department of Materials and Optoelectronic Science, Center for Functional Polymers and Supramolecular Materials, National Sun Yat-Sen University, Kaohsiung 804, Taiwan; Department of Medicinal and Applied Chemistry, Kaohsiung Medical University, Kaohsiung 807, Taiwan;* orcid.org/0000-0002-4306-7171; Email: kuosw@faculty.nsysu.edu.tw

Authors

Swetha V. Chaganti − *Department of Chemistry, National Sun Yat-Sen University, Kaohsiung 80424, Taiwan*

Meng-Syuan Li − *Department of Materials and Optoelectronic Science, Center for Functional Polymers and Supramolecular Materials, National Sun Yat-Sen University, Kaohsiung 804, Taiwan*

Maha Mohamed Samy − *Department of Materials and Optoelectronic Science, Center for Functional Polymers and Supramolecular Materials, National Sun Yat-Sen University, Kaohsiung 804, Taiwan; Department of Chemistry, Faculty of Science, Assiut University, Assiut 71516, Egypt*

Santosh U. Sharma − *Department of Chemistry, National Sun Yat-Sen University, Kaohsiung 80424, Taiwan*

Jyh-Tsung Lee − *Department of Chemistry, National Sun Yat-Sen University, Kaohsiung 80424, Taiwan; Department of Medicinal and Applied Chemistry, Kaohsiung Medical University, Kaohsiung 807, Taiwan;* orcid.org/0000-0002-2658-4222

Mohamed Hammad Elsayed − *Department of Chemical Engineering, National Tsing Hua University, Hsinchu 30013, Taiwan; Department of Chemistry, Faculty of Science, Al-Azhar University, Nasr City 11884 Cairo, Egypt;* orcid.org/0000-0001-7462-0294

Ho-Hsiu Chou − *Department of Chemical Engineering, National Tsing Hua University, Hsinchu 30013, Taiwan;* orcid.org/0000-0003-3777-2277

Complete contact information is available at: https://pubs.acs.org/10.1021/acsaem.2c00942

Author Contributions

[¶]M.G.M. and S.V.C. equally contributed to this work.

Notes

The authors declare no competing financial interest.

ACKNOWLEDGMENTS

This study was supported financially by the Ministry of Science and Technology, Taiwan, under contracts MOST 108-2638-E-002-003-MY2 and 108-2221-E-110-014-MY3. The authors thank the staff at National Sun Yat-sen University for their assistance with the TEM (ID: EM022600) experiments.

REFERENCES

(1) Xiong, S.; Liu, J.; Wang, Y.; Wang, X.; Chu, J.; Zhang, R.; Gong, M.; Wu, B. Solvothermal synthesis of triphenylamine-based covalent organic framework nanofibers with excellent cycle stability for supercapacitor electrodes. *J. Appl. Polym. Sci.* **2022**, *139*, 51510.

(2) Samy, M. M.; Mohamed, M. G.; El-Mahdy, A. F. M.; Mansoure, T. H.; Wu, K. C.-W.; Kuo, S.-W. High-performance supercapacitor electrodes prepared from dispersions of tetrabenzonaphthalene-based conjugated microporous polymers and carbon nanotubes. *ACS Appl. Mater. Interfaces* **2021**, *13*, 51906−51916.

(3) Mohamed, M. G.; Mansoure, T. H.; Samy, M. M.; Takashi, Y.; Mohammed, A. A. K.; Ahamad, T.; Alshehri, S. M.; Kim, J.; Matsagar, B. M.; Wu, K. C.-W.; Kuo, S.-W. Ultrastable Conjugated Microporous Polymers Containing Benzobisthiadiazole and Pyrene Building Blocks for Energy Storage Applications. *Molecules* **2022**, *27*, 2025.

(4) Loganathan, N. N.; Perumal, V.; Pandian, B. R.; Atchudan, R.; Edison, T. N. J. I.; Ovinis, M. Recent studies on polymeric materials for supercapacitor development. *J. Energy Storage* **2022**, *49*, 104149.

(5) Liu, C.; Bai, Y.; Li, W.; Yang, F.; Zhang, G.; Pang, H. In Situ Growth of Three-Dimensional MXene/Metal−Organic Framework Composites for High-Performance Supercapacitors. *Angew. Chem., Int. Ed.* **2022**, *61*, No. e202116282.

(6) Zheng, S.; Li, Q.; Xue, H.; Pang, H.; Xu, Q. A highly alkaline-stable metal oxide@metal−organic framework composite for high-performance electrochemical energy storage. *Natl. Sci. Rev.* **2020**, *7*, 305−314.

(7) Mohamed, M. G.; Sharma, S. U.; Liu, N.-Y.; Mansoure, T. H.; Samy, M. M.; Chaganti, S. V.; Chang, Y.-L.; Lee, J.-T.; Kuo, S.-W. Ultrastable Covalent Triazine Organic Framework Based on Anthracene Moiety as Platform for High-Performance Carbon Dioxide Adsorption and Supercapacitors. *Int. J. Mol. Sci.* **2022**, *23*, 3174.

(8) Liu, S.; Kang, L.; Henzie, J.; Zhang, J.; Ha, J.; Amin, M. A.; Hossain, M. S. A.; Jun, S. C.; Yamauchi, Y. Recent Advances and Perspectives of Battery-Type Anode Materials for Potassium Ion Storage. *ACS Nano* **2021**, *15*, 18931−18973.

(9) Zheng, S.; Sun, Y.; Xue, H.; Braunstein, P.; Huang, W.; Pang, H. Dual-ligand and hard-soft-acid-base strategies to optimize metal-organic framework nanocrystals for stable electrochemical cycling performance. *Natl. Sci. Rev.* **2021**, nwab197.

(10) Liu, S.; Kang, L.; Zhang, J.; Jun, S. C.; Yamauchi, Y. Carbonaceous Anode Materials for Non-aqueous Sodium- and Potassium-Ion Hybrid Capacitors. *ACS Energy Lett.* **2021**, *6*, 4127−4154.

(11) Shaikh, N. S.; Ubale, S. B.; Mane, V. J.; Shaikh, J. S.; Lokhande, V. C.; Praserthdam, S.; Lokhande, C. D.; Kanjanaboos, P. Novel electrodes for supercapacitor: Conducting polymers, metal oxides, chalcogenides, carbides, nitrides, MXenes, and their composites with graphene. *J. Alloys Compd.* **2022**, *893*, 161998.

(12) Liu, S.; Kang, L.; Zhang, J.; Jung, E.; Lee, S.; Jun, S. C. Structural engineering and surface modification of MOF-derived cobalt-based hybrid nanosheets for flexible solid-state supercapacitors. *Energy Storage Mater.* **2020**, *32*, 167−177.

(13) Liu, S.; Kang, L.; Hu, J.; Jung, E.; Zhang, J.; Jun, S. C.; Yamauchi, Y. Unlocking the Potential of Oxygen-Deficient Copper-Doped Co3O4 Nanocrystals Confined in Carbon as an Advanced Electrode for Flexible Solid-State Supercapacitors. *ACS Energy Lett.* **2021**, *6*, 3011−3019.

(14) Kanninen, P.; Luong, N. D.; Sinh, L. H.; Anoshkin, I. V.; Tsapenko, A.; Seppälä, J.; Nasibulin, A. G.; Kallio, T. Transparent and flexible high-performance supercapacitors based on single-walled carbon nanotube films. *Nanotechnology* **2016**, *27*, 235403.

(15) Bai, Y.; Liu, C.; Chen, T.; Li, W.; Zheng, S.; Pi, Y.; Luo, Y.; Pang, H. MXene-Copper/Cobalt Hybrids via Lewis Acidic Molten Salts Etching for High Performance Symmetric Supercapacitors. *Angew. Chem., Int. Ed.* **2021**, *60*, 25318−25322.

(16) Mohamed, M. G.; Samy, M. M.; Mansoure, T. H.; Sharma, S. U.; Tsai, M.-S.; Chen, J.-H.; Lee, J.-T.; Kuo, S.-W. Dispersions of 1,3,4-Oxadiazole-Linked Conjugated Microporous Polymers with Carbon Nanotubes as a High-Performance Electrode for Supercapacitors. *ACS Appl. Energy Mater.* **2022**, *5*, 3677−3688.

(17) Wang, S.; Liu, Y.; Ye, Y.; Meng, X.; Du, J.; Song, X.; Liang, Z. Ultrahigh volatile iodine capture by conjugated microporous polymer based on N, N, N′, N′-tetraphenyl-1, 4-phenylenediamine. *Polym. Chem.* **2019**, *10*, 2608−2615.
(18) Dutta, S.; Bhaumik, A.; Wu, K. C.-W. Hierarchically porous carbon derived from polymers and biomass: effect of interconnected pores on energy applications. *Energy Environ. Sci.* **2014**, *7*, 3574−3592.
(19) Meng, W.-K.; Liu, L.; Wang, X.; Zhao, R.-S.; Wang, M.-L.; Lin, J.-M. Polyphenylene core-conjugated microporous polymer coating for highly sensitive solid-phase microextraction of polar phenol compounds in water samples. *Anal. Chim. Acta* **2018**, *1015*, 27−34.
(20) Wang, H.; Cheng, Z.; Liao, Y.; Li, J.; Weber, J.; Thomas, A.; Faul, C. F. J. Conjugated microporous polycarbazole networks as precursors for nitrogen-enriched microporous carbons for CO_2 storage and electrochemical capacitors. *Chem. Mater.* **2017**, *29*, 4885−4893.
(21) Samy, M. M.; Mohamed, M. G.; Kuo, S.-W. Directly synthesized nitrogen-and-oxygen−doped microporous carbons derived from a bio-derived polybenzoxazine exhibiting high-performance supercapacitance and CO_2 uptake. *Eur. Polym. J.* **2020**, *138*, 109954.
(22) Schmidt, J.; Werner, M.; Thomas, A. Conjugated microporous polymer networks via yamamoto polymerization. *Macromolecules* **2009**, *42*, 4426−4429.
(23) Schmidt, J.; Weber, J.; Epping, J. D.; Antonietti, M.; Thomas, A. Microporous conjugated poly (thienylene arylene) networks. *Adv. Mater.* **2009**, *21*, 702−705.
(24) EL-Mahdy, A. F. M.; Yu, T. C.; Mohamed, M. G.; Kuo, S.-W. Secondary Structures of Polypeptide-Based Diblock Copolymers Influence the Microphase Separation of Templates for the Fabrication of Microporous Carbons. *Macromolecules* **2021**, *54*, 1030−1042.
(25) Gu, C.; Huang, N.; Chen, Y.; Qin, L.; Xu, H.; Zhang, S.; Li, F.; Ma, Y.; Jiang, D. π-conjugated microporous polymer films: designed synthesis, conducting properties, and photoenergy conversions. *Angew. Chem.* **2015**, *127*, 13798−13802.
(26) El-Mahdy, A. F. M.; Young, C.; Kim, J.; You, J.; Yamauchi, Y.; Kuo, S.-W. Hollow microspherical and microtubular [3+3] carbazole-based covalent organic frameworks and their gas and energy storage applications. *ACS Appl. Mater. Interfaces* **2019**, *11*, 9343−9354.
(27) Bezzu, C. G.; Carta, M.; Tonkins, A.; Jansen, J. C.; Bernardo, P.; Bazzarelli, F.; McKeown, N. B. A spirobifluorene-based polymer of intrinsic microporosity with improved performance for gas separation. *Adv. Mater.* **2012**, *24*, 5930−5933.
(28) Du, N.; Park, H. B.; Robertson, G. P.; Dal-Cin, M. M.; Visser, T.; Scoles, L.; Guiver, M. D. Polymer nanosieve membranes for CO_2-capture applications. *Nat. Mater.* **2011**, *10*, 372−375.
(29) Mohamed, M. G.; Atayde, E. C., Jr.; Matsagar, B. M.; Na, J.; Yamauchi, Y.; Wu, K. C.-W.; Kuo, S.-W. Construction hierarchically mesoporous/microporous materials based on block copolymer and covalent organic framework. *J. Taiwan Inst. Chem. Eng.* **2020**, *112*, 180−192.
(30) Mohamed, M. G.; Liu, N.-Y.; EL-Mahdy, A. F. M.; Kuo, S.-W. Ultrastable luminescent hybrid microporous polymers based on polyhedral oligomeric silsesquioxane for CO_2 uptake and metal ion sensing. *Microporous Mesoporous Mater.* **2021**, *311*, 110695.
(31) EL-Mahdy, A. F. M.; Elewa, A. M.; Huang, S. W.; Chou, H. H.; Kuo, S. W. Dual-function fluorescent covalent organic frameworks: HCl sensing and photocatalytic H_2 evolution from water. *Adv. Opt. Mater.* **2020**, *8*, 2000641.
(32) Mohamed, M. G.; Lee, C.-C.; EL-Mahdy, A. F. M.; Lüder, J.; Yu, M.-H.; Li, Z.; Zhu, Z.; Chueh, C.-C.; Kuo, S.-W. Exploitation of two-dimensional conjugated covalent organic frameworks based on tetraphenylethylene with bicarbazole and pyrene units and applications in perovskite solar cells. *J. Mater. Chem. A* **2020**, *8*, 11448−11459.
(33) Samy, M. M.; Mohamed, M. G.; Mansoure, T. H.; Meng, T. S.; Khan, M. A. R.; Liaw, C.-C.; Kuo, S.-W. Solid state chemical transformations through ring-opening polymerization of ferrocene-based conjugated microporous polymers in host−guest complexes with benzoxazine-linked cyclodextrin. *J. Taiwan Inst. Chem. Eng.* **2022**, *132*, 104110.
(34) Li, Y.; Wang, G.; Wei, T.; Fan, Z.; Yan, P. Nitrogen and sulfur co-doped porous carbon nanosheets derived from willow catkin for supercapacitors. *Nano energy* **2016**, *19*, 165−175.
(35) Lu, C.; Tranca, D.; Zhang, J.; Rodríguez Hernández, F.; Su, Y.; Zhuang, X.; Zhang, F.; Seifert, G.; Feng, X. Molybdenum carbide-embedded nitrogen-doped porous carbon nanosheets as electrocatalysts for water splitting in alkaline media. *ACS Nano* **2017**, *11*, 3933−3942.
(36) Xue, D.; Zhu, D.; Xiong, W.; Cao, T.; Wang, Z.; Lv, Y.; Li, L.; Liu, M.; Gan, L. Template-free, self-doped approach to porous carbon spheres with high N/O contents for high-performance supercapacitors. *ACS Sustain. Chem. Eng.* **2019**, *7*, 7024−7034.
(37) Geng, T.; Zhang, C.; Chen, G.; Ma, L.; Zhang, W.; Xia, H. Synthesis of tetraphenylethylene-based fluorescent conjugated microporous polymers for fluorescent sensing and adsorbing iodine. *Microporous Mesoporous Mater.* **2019**, *284*, 468−475.
(38) Mohamed, M. G.; Samy, M. M.; Mansoure, T. H.; Li, C.-J.; Li, W.-C.; Chen, J.-H.; Zhang, K.; Kuo, S.-W. Microporous Carbon and Carbon/Metal Composite Materials Derived from Bio-Benzoxazine-Linked Precursor for CO_2 Capture and Energy Storage Applications. *Int. J. Mol. Sci.* **2022**, *23*, 347.
(39) Elewa, A. M.; EL-Mahdy, A. F. M.; Elsayed, M. H.; Mohamed, M. G.; Kuo, S.-W.; Chou, H.-H. Sulfur-doped triazine-conjugated microporous polymers for achieving the robust visible-light-driven hydrogen evolution. *Chem. Eng. J.* **2021**, *421*, 129825.
(40) Kim, D.; Kang, J.; Yan, B.; Seong, K.-d.; Piao, Y. Ambient Temperature Synthesis of Iron-Doped Porous Nickel Pyrophosphate Nanoparticles with Long-Term Chemical Stability for High-Performance Oxygen Evolution Reaction Catalysis and Supercapacitors. *ACS Sustainable Chem. Eng.* **2020**, *8*, 2843−2853.
(41) Mohamed, M. G.; Chen, T.-C.; Kuo, S.-W. Solid-State Chemical Transformations to Enhance Gas Capture in Benzoxazine-Linked Conjugated Microporous Polymers. *Macromolecules* **2021**, *54*, 5866−5877.
(42) Abuzeid, H. R.; EL-Mahdy, A. F. M.; Kuo, S.-W. Covalent organic frameworks: Design principles, synthetic strategies, and diverse applications. *Giant* **2021**, *6*, 100054.
(43) Mohamed, M. G.; Ahmed, M. M. M.; Du, W.-T.; Kuo, S.-W. Meso/microporous carbons from conjugated hyper-crosslinked polymers based on tetraphenylethene for high-performance CO_2 capture and supercapacitor. *Molecules* **2021**, *26*, 738.
(44) Mohamed, M. G.; EL-Mahdy, A. F. M.; Kotp, M. G.; Kuo, S.-W. Advances in porous organic polymers: syntheses, structures, and diverse applications. *Mater. Adv.* **2022**, *3*, 707−733.
(45) Samy, M. M.; Mohamed, M. G.; Kuo, S.-W. Pyrene-functionalized tetraphenylethylene polybenzoxazine for dispersing single-walled carbon nanotubes and energy storage. *Compos. Sci. Technol.* **2020**, *199*, 108360.
(46) Mohamed, M. G.; Mansoure, T. H.; Takashi, Y.; Mohamed Samy, M.; Chen, T.; Kuo, S.-W. Ultrastable porous organic/inorganic polymers based on polyhedral oligomeric silsesquioxane (POSS) hybrids exhibiting high performance for thermal property and energy storage. *Microporous Mesoporous Mater.* **2021**, *328*, 111505.
(47) Baumann, A. E.; Burns, D. A.; Liu, B.; Thoi, V. S. Metal-organic framework functionalization and design strategies for advanced electrochemical energy storage devices. *Commun. Chem.* **2019**, *2*, 86.
(48) Mehtab, T.; Yasin, G.; Arif, M.; Shakeel, M.; Korai, R. M.; Nadeem, M.; Muhammad, N.; Lu, X. Metal-organic frameworks for energy storage devices: batteries and supercapacitors. *J. Energy Storage* **2019**, *21*, 632−646.
(49) Eftekhari, A.; Fang, B. Electrochemical Hydrogen Storage: Opportunities for Fuel Storage, Batteries, Fuel Cells, and Supercapacitors. *Int. J. Hydrogen Energy* **2017**, *42*, 25143−25165.
(50) Mohamed, M. G.; Elsayed, M. H.; Elewa, A. M.; EL-Mahdy, A. F. M.; Yang, C.-H.; Mohammed, A. A. K.; Chou, H.-H.; Kuo, S.-W. Pyrene-containing conjugated organic microporous polymers for

https://doi.org/10.1021/acsaem.2c00942
ACS Appl. Energy Mater. 2022, 5, 6442−6452

photocatalytic hydrogen evolution from water. *Catal. Sci. Technol.* **2021**, *11*, 2229−2241.
(51) Wei, Z.; Wang, D.; Liu, Y.; Guo, X.; Zhu, Y.; Meng, Z.; Yu, Z.-Q.; Wong, W.-Y. Ferrocene-based hyperbranched polymers: a synthetic strategy for shape control and applications as electroactive materials and precursor-derived magnetic ceramics. *J. Mater. Chem. C* **2020**, *8*, 10774−10780.
(52) Zhang, H.; Zhang, Y.; Gu, C.; Ma, Y. Electropolymerized conjugated microporous poly (zinc-porphyrin) films as potential electrode materials in supercapacitors. *Adv. Energy Mater.* **2015**, *5*, 1402175.
(53) Kou, Y.; Xu, Y.; Guo, Z.; Jiang, D. Supercapacitive energy storage and electric power supply using an aza-fused π-conjugated microporous framework. *Angew. Chem., Int. Ed.* **2011**, *123*, 8912−8916.
(54) Thomas, A.; Kuhn, P.; Weber, J.; Titirici, M.-M.; Antonietti, M. Porous Polymers: Enabling Solutions for Energy Applications. *Macromol. Rapid Commun.* **2009**, *30*, 221−236.
(55) Xu, M.; Zhang, S.; Wang, T.; Yu, B.; Yang, Z.; Wang, X.; Zhou, R.; Hua, D. De Novo Design of a Pt Nanocatalyst on a Conjugated Microporous Polymer-Coated Honeycomb Carrier for Oxidation of Hydrogen Isotopes. *ACS Appl. Mater. Interfaces* **2022**, *14*, 7826−7835.
(56) Giri, A.; Biswas, S.; Hussain, M. W.; Dutta, T. K.; Patra, A. Nanostructured Hypercrosslinked Porous Organic Polymers: Morphological Evolution and Rapid Separation of Polar Organic Micropollutants. *ACS Appl. Mater. Interfaces* **2022**, *14*, 7369−7381.
(57) Jiang, J.-X.; Wang, C.; Laybourn, A.; Hasell, T.; Clowes, R.; Khimyak, Y. Z.; Xiao, J.; Higgins, S. J.; Adams, D. J.; Cooper, A. I. Metal−organic conjugated microporous polymers. *Angew. Chem., Int. Ed.* **2011**, *50*, 1072−1075.
(58) Bojdys, M. J.; Wohlgemuth, S. A.; Thomas, A.; Antonietti, M. Ionothermal route to layered two-dimensional polymer-frameworks based on heptazine linkers. *Macromolecules* **2010**, *43*, 6639−6645.
(59) Wang, X.; Maeda, K.; Thomas, A.; Takanabe, K.; Xin, G.; Carlsson, J. M.; Domen, K.; Antonietti, M. A metal-free polymeric photocatalyst for hydrogen production from water under visible light. *Nat. Mater.* **2009**, *8*, 76−80.
(60) Zhu, Z.; Yang, Z.; Fan, Y.; Liu, C.; Sun, H.; Liang, W.; Li, A. Calcination of Porphyrin-Based Conjugated Microporous Polymers Nanotubes As Nanoporous N-Rich Metal-Free Electrocatalysts for Efficient Oxygen Reduction Reaction. *ACS Appl. Energy Mater.* **2020**, *3*, 5260−5268.
(61) Thomas, A. Functional materials: from hard to soft porous frameworks. *Angew. Chem., Int. Ed.* **2010**, *49*, 8328−8344.
(62) Chen, L.; Honsho, Y.; Seki, S.; Jiang, D. Light-harvesting conjugated microporous polymers: rapid and highly efficient flow of light energy with a porous polyphenylene framework as antenna. *J. Am. Chem. Soc.* **2010**, *132*, 6742−6748.
(63) Xie, Z.; Wang, C.; DeKrafft, K. E.; Lin, W. Highly stable and porous cross-linked polymers for efficient photocatalysis. *J. Am. Chem. Soc.* **2011**, *133*, 2056−2059.
(64) Mohamed, M. G.; Sharma, S. U.; Yang, C.-H.; Samy, M. M.; Mohammed, A. A. K.; Chaganti, S. V.; Lee, J.-T.; Wei-Kuo, S. Anthraquinone-Enriched Conjugated Microporous Polymers as Organic Cathode Materials for High-Performance Lithium-Ion Batteries. *ACS Appl. Energy Mater.* **2021**, *4*, 14628−14639.
(65) Jiang, J.-X.; Su, F.; Trewin, A.; Wood, C. D.; Campbell, N. L.; Niu, H.; Dickinson, C.; Ganin, A. Y.; Rosseinsky, M. J.; Khimyak, Y. Z.; Cooper, A. I. Conjugated microporous poly (aryleneethynylene) networks. *Angew. Chem.* **2007**, *119*, 8728−8732.
(66) Boota, M.; Chen, C.; Bécuwe, M.; Miao, L.; Gogotsi, Y. Pseudocapacitance and excellent cyclability of 2, 5-dimethoxy-1, 4-benzoquinone on graphene. *Energy Environ. Sci.* **2016**, *9*, 2586−2594.
(67) Chen, W.-C.; Wen, T.-C.; Teng, H. Polyaniline-deposited porous carbon electrode for supercapacitor. *Electrochim. Acta* **2003**, *48*, 641−649.
(68) Rafik, F.; Gualous, H.; Gallay, R.; Crausaz, A.; Berthon, A. Frequency, thermal and voltage supercapacitor characterization and modeling. *J. Power Sources* **2007**, *165*, 928−934.
(69) Weng, Z.; Su, Y.; Wang, D.-W.; Li, F.; Du, J.; Cheng, H.-M. Graphene−cellulose paper flexible supercapacitors. *Adv. Energy Mater.* **2011**, *1*, 917−922.
(70) Xu, R.; Guo, F.; Cui, X.; Zhang, L.; Wang, K.; Wei, J. High performance carbon nanotube based fiber-shaped supercapacitors using redox additives of polypyrrole and hydroquinone. *J. Mater. Chem. A* **2015**, *3*, 22353−22360.

https://doi.org/10.1021/acsaem.2c00942
ACS Appl. Energy Mater. 2022, 5, 6442−6452